

Electrical Properties Characterization of AlGa_N/Ga_N MODFET

¹S. Das, ²R. K. Nayak, ³G. N. Dash ⁴A. K. Panda

^{1,2,4} National Institute of Science and Technology, Palur Hills, Berhampur, Odisha, India – 761008.

³School of Physics, Sambalpur University, Odisha, India-768019.

Abstract: The electrical properties characterization of AlGa_N/Ga_N based Modulation Doped Field Effect Transistor (MODFET) is reported. Threshold voltage $V_{th} = -3.87$ V, maximum saturation current $I_{dss} = 122.748$ mA, gate-source capacitance at zero gate voltage and also maximum gate-source capacitance = 0.161753 pF/ μ m, gate-source capacitance = 0.157233 pF/ μ m at $I_d = 0.3I_{dss}$, trans-conductance (g_m) = 31.3806 mS/mm at zero gate voltage, maximum trans-conductance (g_{max}) = 31.765 mS/mm, trans-conductance (g_m) = 30.351 mS/mm at $I_d = 0.3I_{dss}$ has been achieved. The dependence of Two-Dimensional Electron Gas (2-DEG) density at the interface on Al mole fraction and thickness of AlGa_N barrier layer is also presented.

Keywords: MODFET, 2-DEG, SILVACO TCAD, Mole fraction, Critical Thickness.

Introduction

In recent years, developments of microwave power transistors have helped to realize efficient communication systems involving a wide range of frequency of operation [1-4]. Microwave power transistors made of conventional semiconductors have already approached their performance limit. In order to meet the future needs of wireless communication systems, a great amount of effort is being put on microwave power devices like MODFET, HBT (Hetero-junction Bipolar Transistor) etc. based on wide band gap semiconductors, among which the III-nitride based MODFETs are emerging as the potential candidate because of their exceptional power handling capability [5]. There have been considerable efforts to scale dimensions in III-nitride MODFETs to improve high-frequency performance of the transistors. At the same time efforts are being put on reducing the various non-ideal effects introduced due to device scaling. These include gate recessing to increase the device aspect ratio [6], the use of a double hetero-junction structures [7], and inverted MODFET structures based on the N-polar orientation of wurtzite Ga_N (which exploits the reversed direction of spontaneous and piezoelectric polarization effects) [8]. In the last two decades, the AlGa_N/Ga_N MODFETs have achieved exceptional improvements in their performance. The inherent material properties such as high breakdown field, high mobility and saturated velocity, high thermal conductivity, and wide band gap make AlGa_N/Ga_N MODFET a promising candidate for many microwave power applications. The combination of improved growth technology and device fabrication mechanisms have enabled devices to generate a power density up to 9.2 W/mm at 8 GHz and 30 V bias for AlGa_N/Ga_N MODFET with SiC as substrate. This is about ten times more than GaAs-based FETs and is thus well beyond the capability of GaAs FETs [9]. An outstanding output power performance of 40 W/mm at 4 GHz [10], a unity current gain cutoff frequency of 160 GHz [11], and a maximum frequency of oscillation of 300 GHz [12] are some noteworthy features of AlGa_N/Ga_N MODFET performance. The cutoff frequency f_T of state-of-the-art AlGa_N/Ga_N MODFETs reaches a value of 190 GHz for a gate length $L = 60$ nm [13]. With combined merits of high power and high saturation velocity [14], MODFETs made of AlGa_N/Ga_N material combination are suitable for both electronic and optoelectronic devices. An excellent high-frequency performance, with a current gain cut-off frequency (f_T) of 153 GHz and power gain cut-off frequency (f_{max}) of 198 GHz for a gate length of 100 nm for an AlGa_N/Ga_N MODFET using Ga_N/ultrathin InGa_N/Ga_N hetero-junction as a back-barrier to the electrons in the structure have been reported [15]. The realization of high-performance 0.1 - μ m gate AlGa_N/Ga_N MODFET grown on high-resistivity silicon substrates with features like cutoff frequencies as high as $f_T = 75$ GHz and $f_{max} = 125$ GHz are the highest values reported so far for AlGa_N/Ga_N MODFETs on silicon [16]. Recent intensive research on AlGa_N/Ga_N MODFETs has resulted in monolithic integration of two III-nitride device structures - one with enhancement-mode (E-mode) and the other with depletion-mode (D-mode) AlN/GaN/AlGa_N double-heterojunction field-effect transistors (DHFETs) on a single SiC substrate through the use of etching and regrowth by molecular beam epitaxy (MBE). D-mode devices with a gate length of 150 nm had a threshold voltage V_{th} of -0.10 V, a peak transconductance g_m value of 640 mS/mm, and current-gain and power-gain cutoff frequencies f_T and f_{max} of 82 and 210 GHz, respectively. E-mode devices on the same wafer with the same dimensions had a V_{th} value of $+0.24$ V, a peak g_m value of 525 mS/mm, and f_T and f_{max} values of 50 and 150 GHz, respectively [17]. Also

very accurate analytical models for the device are reported in literatures [18-20]. The electrical properties required for simulation purpose of $\text{Al}_x\text{Ga}_{1-x}\text{N}$ ($x=0.3$) and GaN is tabulated in Tables 1 and 2, respectively [21]. These reports have established that AlGaIn/GaN material system has excellent potential for MODFET application. It has thus opened up avenues for deeper study on this material based system for MODFET applications. The main aim of this paper is to compare the results obtained through simulation using SILVCO TCAD tool by taking structures of MODFET (namely a single hetero-junction AlGaIn/GaN MODFET) with the experimental results available in the literature. The simulation has been done by changing different parameters, DC characteristics curve, transfer characteristics curve, transconductance curves, gate to source capacitance curve have been traced for the device. The basic MODFET structure and models used for simulation are described in Section 2. In section 3, the various simulation results are discussed. The paper is concluded in Section 4.

I. Methods Developed For Algan/Gan Interface Properties

A novel method has been developed for the study of AlGaIn/GaN interface properties and is presented in this section. Energy band diagrams and different other results obtained for the GaN-based hetero-structures are obtained by using a computer program developed by authors. This computer program solves self-consistently the Schrödinger's and Poisson's equations for the electron wave functions using Finite Difference Method (FDM) and LU-Decomposition. The solution gives a detailed knowledge of electron and hole concentrations in the hetero-structures which are used to study the energy band diagrams and interfacial characteristics of hetero-structures. The finite difference method (FDM) is a simple and efficient method for solving ordinary differential equation with simple boundary conditions. FDM can be used to solve for the Schrödinger's equation. Real space is divided into discrete mesh points and the wave function is solved within those discrete spacing. The method requires the construction of mesh defining local coordinate surfaces. For each node of this mesh, the unknown wave function values are found by replacing the differential equation by difference equation. These values give the vector solution for wave function Ψ and a matrix formulation of the Schrödinger equation as:

$$A\Psi = \lambda\Psi \quad (1)$$

where A is the matrix operator and λ is the energy eigen values. Usually a uniform mesh size is selected but this method will not be effective. We need a small mesh when the wave function is changing rapidly and a large mesh during a slow change in the wave function for the ideal solution. Moreover, careful calculations are also required at the junction of two different mesh sizes and destroying the symmetry of matrix A , making it more difficult to calculate. First both the Schrödinger's equation and Poisson's equation are expressed in tridiagonal matrix form using FDM technique. Then LU-Decomposition method is being used to get the potential solution of the Poisson's equation. The inverse iteration method is used to solve the Schrödinger's equation to get the eigen values and corresponding eigenvectors. Then the solutions of the Schrödinger's equation and the Poisson's equation are self consistently solved to get the final potential and electron distribution. A brief description for solving Schrödinger's equation and Poisson's equation self-consistently is given below. The one-dimensional, one electron Schrödinger equation within effective mass theory (EMA) is given as

$$-\frac{\hbar^2}{2} \frac{d}{dx} \left(\frac{1}{m^*(x)} \frac{d}{dx} \right) \Psi(x) + V(x)\Psi(x) = E\Psi(x) \quad (2)$$

where \hbar is reduced Plank's constant, m^* is the electron effective mass, $\Psi(x)$ is the wave function, E is the eigen energy and $V(x)$ is the potential energy. Solving the equation (2) in matrix form using FDM technique, the wave functions ($\Psi_k(x)$), corresponding eigen values (E_k) and fermi energy (E_f) is obtained. The electron concentration for k^{th} sub-band per unit area is given by

$$n_k = \int_{E_k}^{\infty} g(E) f(E) dE \quad (3)$$

where $f(E)$ is the Fermi-Dirac distribution function given by

$$f(E) = \frac{1}{1 + \exp[(E - E_f)/KT]} \quad (4)$$

and $g(E)$ is the 2-D density of states for a single sub-band in a quantum well system given by

$$g(E) = \frac{m^*}{\pi\hbar^2} \quad (5)$$

Using equations (3), (4) and (5), we get

$$n_k = \frac{m^*}{\pi\hbar^2} \int_{E_k}^{\infty} \frac{1}{1 + \exp(E - E_f)/KT} \quad (6)$$

where K is the Boltzmann constant and T is temperature in Kelvin.

The wave function $\Psi_k(x)$ is related to the electron density per unit area $n'(x)$ inside the structure given by

$$n'(x) = \sum_{k=1}^m \Psi_k^*(x) \Psi_k(x) n_k \quad (7)$$

$$n'(x) = \sum_{i=1}^m \frac{m^* K T}{\pi\hbar^2} \ln[1 + \exp(E_f - E_k)/KT] |\Psi_k(x)|^2 \quad (8)$$

where m is the number of bound states, $\Psi_k(x)$ is the position dependent wave function and $\Psi_k^*(x)$ is the complex conjugate of $\Psi_k(x)$.

The $n'(x)$ distribution obtained above after expressed in per unit volume as $n(x)$ is now being put in the 1-D Poisson equation given by

$$\frac{d}{dx} \left(\epsilon_s(x) \frac{d}{dx} \right) \phi(x) = \frac{-q[N_D(x) - n(x)]}{\epsilon_o} \quad (9)$$

where $\epsilon_s(x)$ is the position dependent dielectric constant, $\phi(x)$ is the electrostatic potential and $N_D(x)$ is the ionized donor concentration and $n(x)$ is the electron density distribution per unit volume. Solving the equation (3) in matrix form again using FDM technique, an electrostatic potential $\phi(x)$ is obtained.

This $\phi(x)$ is used to calculate the updated new potential energy distribution as

$$V_{out}(x) = f_i[-q\phi(x) + V_0(x)] + V_0(x) + \Delta E_c \quad (10)$$

where ΔE_c is the pseudo potential energy due to the conduction band offset at the hetero-junction, $V_0(x)$ is the potential energy distribution used in the present iteration and f_i is the scaling factor ranging from 0.05 to 0.1.

For AlGaIn/GaN material, the total polarization charge at the interface must be taken into account in the Poisson equation for calculations of the sheet carrier concentration as $E_{AlGaIn}\epsilon_{AlGaIn} - E_{GaN}\epsilon_{GaN} = -\sigma$ where E is the electric field, ϵ is the dielectric constant and σ is the polarization charge density at the interface. The total polarization charge can also be written as $P_{TOTAL} = P_{PZ} + P_{SP}$, where P_{PZ} is the piezoelectric charge caused by the lattice mismatch and by the thermal strain given by $P_{PZ} = P_{MIS} + P_{TS}$ where P_{MIS} is the piezoelectric charge due to lattice mismatch and P_{TS} is the piezoelectric charge due to thermal strain, whereas P_{SP} represents the spontaneous polarizability of the GaN/AlGaIn interface, as clearly demonstrated by the works of Bernardini et al. [22]. Actually the piezoelectric and spontaneous polarization charge is inextricable from the gate-induced and charge induced by doping in barrier layer and so it must be carefully considered in device design and analysis.

These are the basic equations required to solve for finding the solution to the Schrödinger's equation and Poisson's equations self-consistently.

The procedure of our algorithm is then divided into the following steps:

- [1]. We start with a trial potential energy value of $V_0(x)$ and then calculate the wave functions $\Psi(x)$ and the corresponding eigen energies E_k using matrix representation of Schrödinger's wave equation (2) using FDM method.
- [2]. Then the values associated with n_k are found out using the equation (6).

- [3]. Then the electron density distribution $n'(x)$ is calculated by using the equations given for $n'(x)$ above as (8).
- [4]. The above calculated value of $n'(x)$ is then expressed in per unit volume $n(x)$ and along with the given donor concentration $N_D(x)$ and total polarization charge P_{TOTAL} , 1-D Poisson's equation (9) is solved to obtain $\phi(x)$ and from this a new potential energy $V(x)$ is obtained using the equation (10).
- [5]. Again we use this new value of $V(x)$ in the Schrödinger's equation to find new values of wave function $\Psi(x)$ and the corresponding Eigen energies E_k .

In this way, the iterations will continue till it yields self-consistent solutions for $V(x)$ and $n(x)$ i.e. the iteration is repeated until convergence is achieved. After getting the self-consistent solutions for $V(x)$ and $n(x)$, these values of $V(x)$ and $n(x)$ can be used to determine the band diagram as well as carrier concentration in the channel.

II. MODFET Structure And Its Simulation Model

The MODFET structure for simulation is shown in figure 1. The epitaxial layers consists of a 0.015 μm n-doped Al_xGa_{1-x}N layer where $x=0.3$ with doping concentration $N_D = 10^{18} \text{ cm}^{-3}$, a 0.005 μm unintentionally doped Al_xGa_{1-x}N spacer layer and a 1 μm thick, undoped, high resistivity GaN buffer layer grown on Sapphire substrate along (0001) plane with a nucleation layer of thickness 0.007 μm in between these two layers. AlN nucleation layer is required to control the GaN polarity. The thick buffer layer is employed to spatially remove the active part of the device from the higher-defect-density material near the substrate interface. The device width is taken as 50 μm , length is of 3.6 μm and depth is 6 μm . The gate length (L_g) is of 0.3 μm , distance between source to gate (L_{sg}) is 0.7 μm and drain to gate (L_{dg}) is 2 μm , distance between drain and source (L_{ds}) is 3 μm and length of drain (L_d) and source (L_s) is 0.3 μm . The drain and source is n-doped. The drain and source are having ohmic contacts and gate is having Schottky contact with work function of 4.3eV[23]. Figure 2 represents the 2D representation of the modeled AlGa_x/GaN HEMT and figure 3 represents the meshed structure of AlGa_x/GaN MODFET. Figure 4 represents the carrier concentration level in simulated device. Non-linear iteration solution method used in the simulations is the Newton-Raphson iteration method [24]. A low field mobility model is used following the work of Albrecht et al. [25]. The transport model used here is Energy Balance Transport Model [23, 26]. Recombination Model used is Chuang's Three Band Model for Radiative Recombination in Wurtzite Materials [27]. The impact ionization and tunneling parameters have not been included in the simulation due to their rather negligible effects on the device characteristics below breakdown. To produce the polarization effects in device we have taken interface charge of approximate $0.99 \times 10^{13} \text{ C/cm}^2$ at the hetero-junction interface [21].

III. Results and Discussion

3.1 DC Characteristics

The MODFET device is simulated with an $x=0.3$ Al mole fraction under different gate biases. Figure 5 represents the simulated I-V characteristic of the device for different gate voltages. Output characteristics of the MODFET device is simulated using Silvaco ATLAS simulation tool for $V_d=0$ to 15V and $V_g= 0$ to -5. The simulated I-V curves have noticeable differences. While the real device peaks at 5V on the drain, only the -5V gate bias case does so in the model. The real device never surpasses about 0.0009 amps while the model approaches 0.0012 Amps. The real device curves (except the -5V gate bias case) begin to fall off around 13V on the drain, but the model drain current never fall off. This inconsistency is expected to be caused by heating effects for which the model does not account. The simulated result is compared with measured results and found to be in good agreement with it [28].

3.2 Transfer characteristics

Figure 6 represents the simulated transfer characteristic curve of the modeled MODFET device for $V_g = 1$ to -10V with $V_d = 15\text{V}$. The transfer characteristic is used to obtain the threshold voltage (V_{th}) which is found to be -3.87V and saturation drain current, I_{dss} as 122.748mA. These results are in good agreement with experimental results [28].

3.3 Transconductance (g_m)

Figure 7 represents the simulated drain-gate trans-conductance curve of the modeled MODFET device. Starting at a high negative gate bias, the trans-conductance increases with increase in V_{gs} as there is increase in charge in the channel. After going through a peak i.e. 31.765 mS/mm, it starts decreasing with increase in V_{gs} as the applied gate bias begins to produce charge transport in the AlGa_xN layer. From the curve, the trans-

conductance found is of the value of $g_m=31.3806\text{mS/mm}$ at $V_g=0$ and $g_m=30.351\text{mS/mm}$ at $I_d=0.3I_{dss}$. These values are found to be in good agreement with experimentally found results [28].

3.4 Gate-to-source capacitance (C_{gs})

Figure 8 represents the simulated gate-to-source capacitance curve. Gate to source capacitance at $V_g=0$ is $C_{gs}=1.61753 \times 10^{-13} \text{ F}/\mu\text{m}$; gate to source capacitance at $I_d=0.3I_{dss}$ is $C_{gs}=1.57233 \times 10^{-13} \text{ F}/\mu\text{m}$; and maximum gate to source capacitance is found to be $C_{gs(\text{max})}=1.61753 \times 10^{-13} \text{ F}/\mu\text{m}$. These results are compared with experimentally found results [28] which show a good agreement between the two.

3.5 Effect of AlGaIn layer Thickness on the Sheet Carrier Density

Figure 9 shows the variation of 2-DEG density as a function of thickness of $\text{Al}_{0.3}\text{Ga}_{0.7}\text{N}$ layer. As we can see from the figure, the 2-DEG density starts increasing rapidly after a certain thickness of the AlGaIn layer. This thickness is called the critical thickness t_{CR} (here the critical thickness is found to be around 35 \AA). The critical thickness depends on factors such as the alloy composition and the doping concentration of the layers.

3.6 Effect of Al Mole Fraction in AlGaIn/GaN Structures

The dependence of sheet carrier density on the alloy composition value x is shown in figure 10 which shows that as the value of alloy composition is increased, the sheet density also increases and almost has a linear relationship between the two. This result is consistent with the Hall measurements of Lu et al. [29].

IV. Conclusion

In this paper, the electrical properties characterization of AlGaIn/GaN based MODFET is reported and simulated I-V and C-V characteristic curves are obtained for the above mentioned MODFET structure using SILVCO TCAD tool. The results, threshold voltage $V_{th} = -3.87 \text{ V}$, maximum saturation current $I_{dss} = 122.748 \text{ mA}$, gate-source capacitance at zero gate voltage and also maximum gate-source capacitance of value $0.161753 \text{ pF}/\mu\text{m}$, gate-source capacitance of $0.157233 \text{ pF}/\mu\text{m}$ at $I_d=0.3I_{dss}$, transconductance (g_m) = 31.3806 mS/mm at zero gate voltage, maximum transconductance (g_{max}) = 31.765 mS/mm and transconductance of value 30.351 mS/mm at $I_d = 0.3I_{dss}$ has been achieved. The sheet carrier concentration increases almost linearly with the increase of Al mole fraction. These results show good agreement with the experimental data over the almost full range of gate and drain biases.

References

- [1] Ekaterina Harvard, Richard Brown, James R. Shealy, IEEE Trans. Electron Devices 58 (2011) 87.
- [2] Eric R. Heller, Rama Vetury, Daniel S. Green, IEEE Trans. Electron Devices 58 (2011) 1091.
- [3] Masataka Higashiwaki, YiPei, Rongming Chu, IEEE Trans. Electron Devices 58 (2011) 1681.
- [4] Ya-Lan Chiou, Ching-Ting Lee, IEEE Trans. Electron Devices 58 (2011) 3869.
- [5] L. F. Eastman, U. K. Mishra, IEEE Spectr. 39 (2002) 28.
- [6] A. Kuliev, Solid State Electron. 47 (2003) 117.
- [7] M. Micovic, P. Hashimoto, M. Hu, IEDM Tech. Dig. (2004) 807.
- [8] S. Rajan, A. Chini, M. H. Wong, J. Appl. Phys. 102 (2007) 044 501.
- [9] S. T. Sheppard, K. Doverspike, W. L. Pribble, IEEE Electron Device Lett. 20 (1999) 161.
- [10] D. Kim, V. Kumar, J. Lee, IEEE Electron Device Lett. 30 (2009) 913.
- [12] J. W. Chung, W. E. Hoke, E. M. Chumbes, IEEE Electron Device Lett. 31 (2010) 195.
- [13] M. Higashiwaki, T. Mimura, T. Matsui, Appl. Phys. Express. 1 (2008) 021 103.
- [14] C. H. Oxley, M. J. Uren, A. Coates, IEEE Trans. Electron Devices 53 (2006) 565.
- [15] T. Palacios, A. Chakraborty, S. Heikman, IEEE Electron Device Lett. 27 (2006) 13.
- [16] Haifeng Sun, Andreas R. Alt, Hansruedi Benedikter, IEEE Electron Device Lett. 30 (2009) 107.
- [17] D. F. Brown, K. Shinohara, A. Williams, I. Milosavljevic, R. Grabar, P. Hashimoto, P. J. Willadsen, A. Schmitz, A. L. Corion, S. Kim, D. Regan, C. M. Butler, S. D. Burnham, M. Micovic, IEEE Trans. Electron Devices 58 (2011) 1063.
- [18] Xiaoxu Cheng, Yan Wang, IEEE Trans. Electron Devices 58 (2011) 448.
- [19] Michele Esposito, Alessandro Chini, Siddharth Rajan, IEEE Trans. Electron Devices 58 (2011) 1456.
- [20] Sivakumar Mudanai, Ananda Roy, Roza Kotlyar, Titash Rakshit, Mark Stettler, IEEE Trans. Electron Devices 58 (2011) 4204.
- [21] O Ambacher, J. Phys.D: Appl. Phys. 31 (1998) 2653.
- [22] F. Bernardini, V. Fiorentini, D. Vanderbilt, Phys. Rev. (1997) B 56 R10024.
- [23] M. Lundstrom, Fundamental of Carrier Transport, 2nd ed., Cambridge University Press, New York (2000).
- [24] D.H. Rose, R.E. Bank, Numerische Mathematik 37 (1981) 279.
- [25] J.D. Albrecht, J. Appl. Phys. 83 (1998) 4777.
- [26] C.R. Crowell, S. M. Sze, Solid State Electronics 9 (1966) 1035.
- [27] Chuang S. L, IEEE J. of Quantum Elec. 32 (1996) 1791.
- [28] Y.-F. Wu, S. Keller, P. Kozodoy, B.P. Parikh, D. Kapolnek, S.P. Denbaars, IEEE Electron Device Lett. 18 (1997) 290.
- [29] Wu Lu, Vipin Kumar, Edwin L. Piner, IEEE Trans. Electron Devices 50 (2003) 1069.

Captions To Table:

Table 1. Material properties of Al_xGa_{1-x}N (x=0.3) at room temperature

Table 2. Material properties of GaN at room temperature

Captions To Figures:

Figure 1. Structure and different dimensions of simulated AlGa_xGa_{1-x}N MODFET

Figure 2. 2D representation of the modeled AlGa_xGa_{1-x}N MODFET using SILVACO TCAD

Figure 3. Meshed structure of the modeled AlGa_xGa_{1-x}N MODFET using SILVACO TCAD

Figure 4. Concentration level in simulated AlGa_xGa_{1-x}N MODFET using SILVACO TCAD

Figure 5. Output characteristics of the modeled MODFET device for V_d= 0 to 15V and V_g= 0 to -5V

Figure 6. Input transfer characteristics of the modeled MODFET device for V_g= 1 to -10V with V_d=15V

Figure 7. Drain-Gate trans-conductance vs gate voltage

Figure 8. Gate-Source capacitance vs gate voltage

Figure 9. Simulated values for 2DEG density Vs Al_{0.3}Ga_{0.7}N thickness

Figure 10. Sheet carrier density in AlGa_xGa_{1-x}N structure as a function of Al_xGa_{1-x}N barrier composition x

Material: Al_xGa_{1-x}N (x=0.3)	
Electron mobility	600 cm ² V ⁻¹ s ⁻¹
Hole mobility	10 cm ² V ⁻¹ s ⁻¹
Electron Affinity	3.82 eV
Conduction band density of states (N _c at T=300K)	2.07x10 ¹⁸ cm ⁻³
Valence band density of states (N _v at T=300K)	1.16x10 ¹⁹ cm ⁻³
Energy gap (E _g)	3.96eV
Alignment	0.8eV
Relative Permittivity	10.32

Table 1 S Das et al.

Material: GaN	
Electron mobility	900 cm ² V ⁻¹ s ⁻¹
Hole mobility	10 cm ² V ⁻¹ s ⁻¹
Conduction band density of states (N _c at T=300K)	1.07x10 ¹⁸ cm ⁻³
Valence band density of states (N _v at T=300K)	1.16x10 ¹⁹ cm ⁻³
Energy gap (E _g)	3.4eV
Alignment	0.8eV
Relative Permittivity	9.5

Table 2 S Das et al.

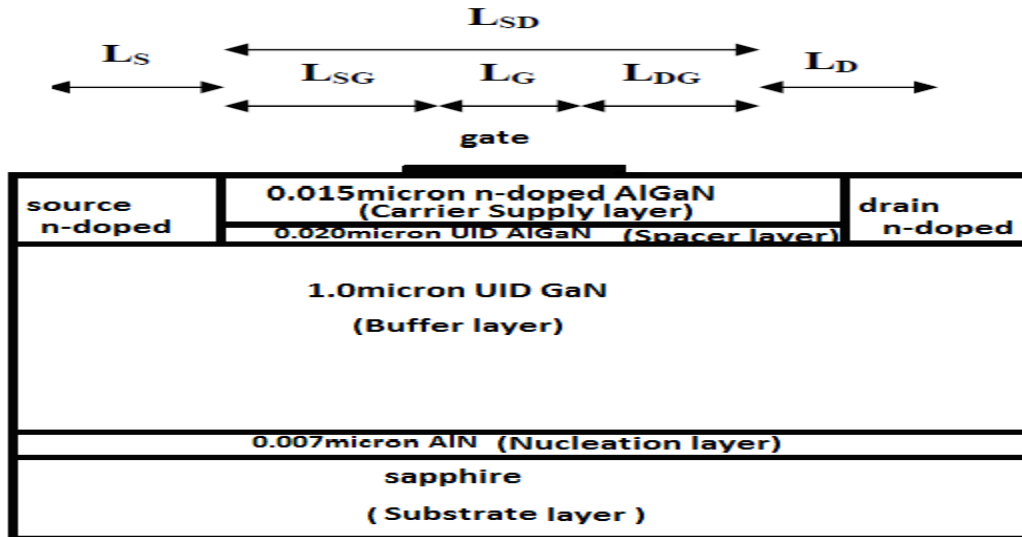


Figure 1 S Das et al.

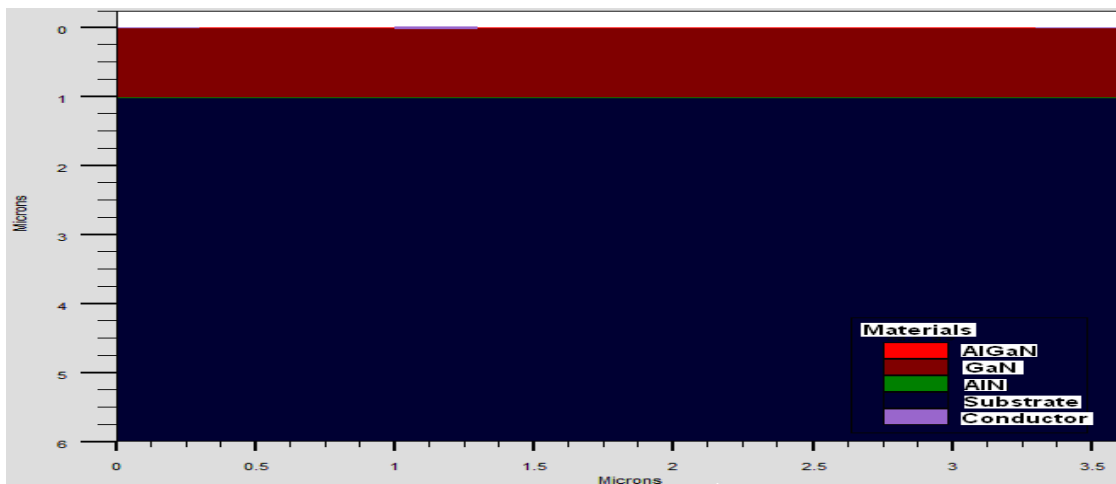


Figure 2 S Das et al.

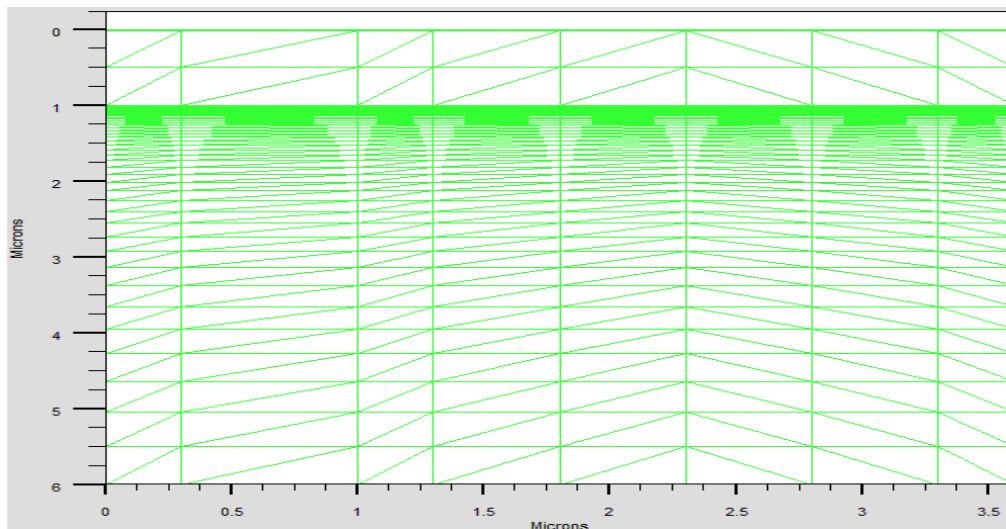


Figure 3 S Das et al.

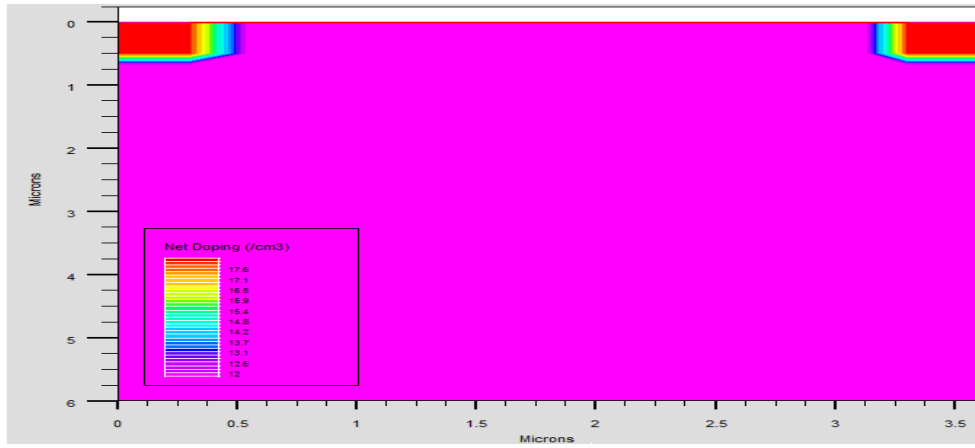


Figure 4 S Das et al.

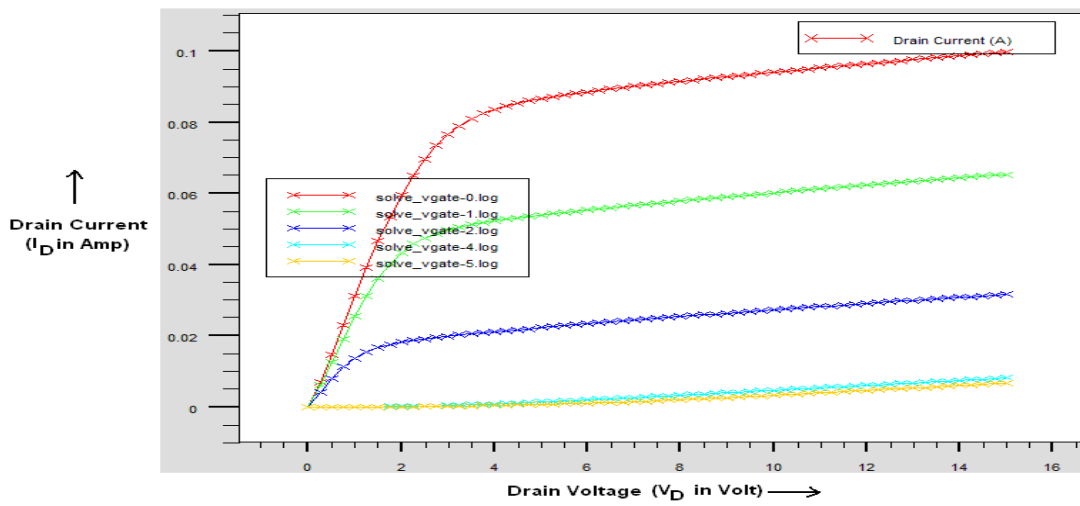


Figure 5 S Das et al.

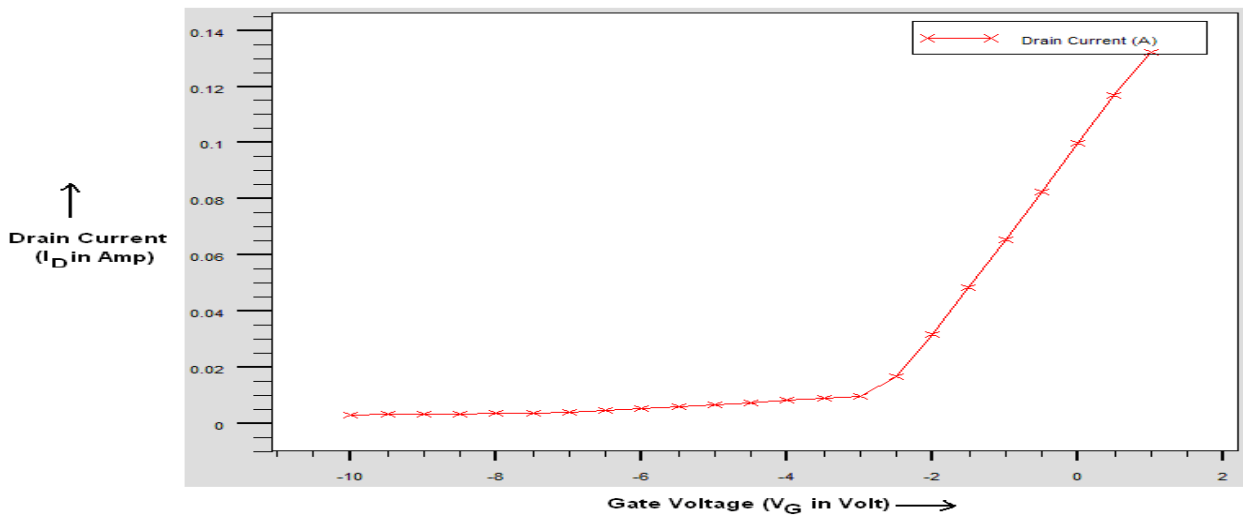


Figure 6 S Das et al.

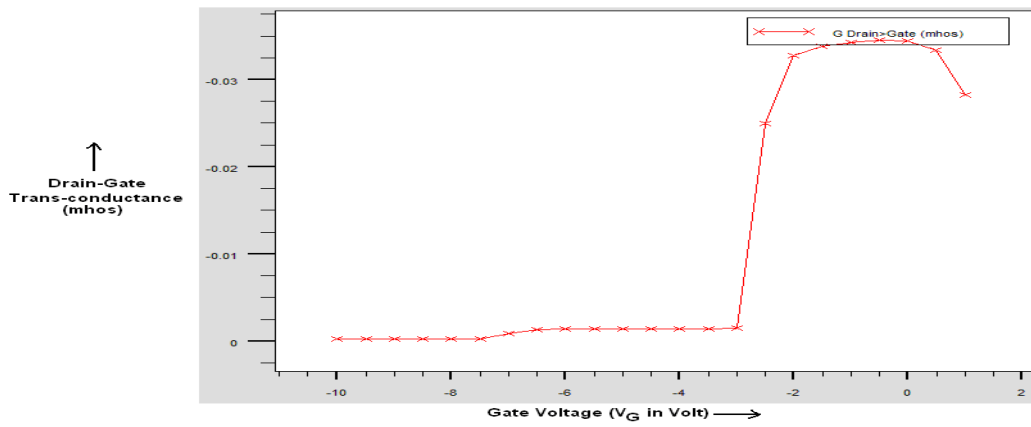


Figure 7 S Das et al.

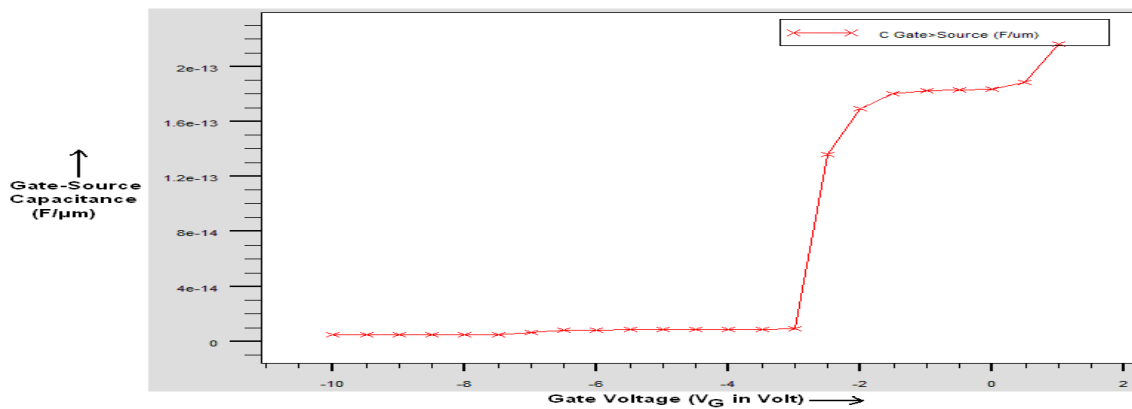


Figure 8 S Das et al.

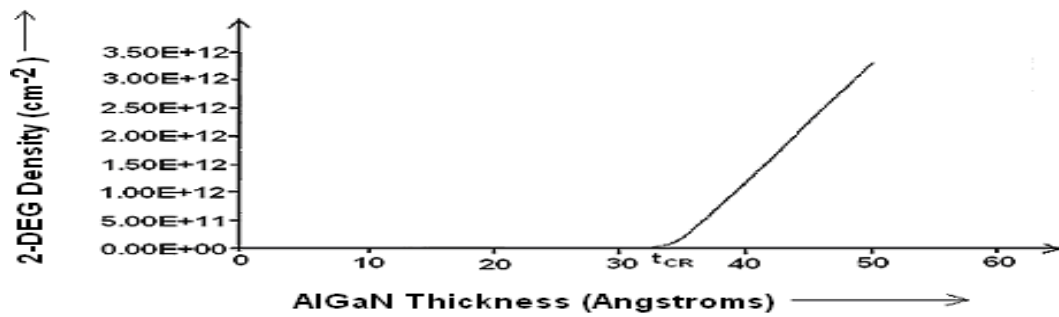


Figure 9 S Das et al.

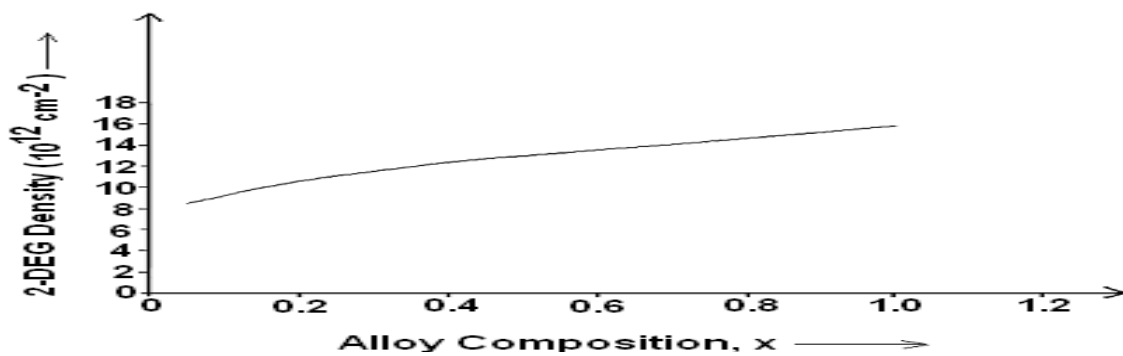


Figure 10 S Das et al.